energies

MDPI

Article

Optimal Operation of Grid-Forming-Controlled PV and Energy Storage Converters in Low-Voltage Distribution Networks

Xuguang Zhou [1], Jian Han [2,*], Bo Chen [1], Shuocheng Wang [1], Simeng Cheng [1], Zaide Xu [1] and Zhirui Yang [2]

[1] State Grid Jiangxi Electric Power Research Institute, Nanchang 331000, China; zhouxg_2013@126.com (X.Z.); orchis1986@126.com (B.C.); wangsc2010@126.com (S.W.); 13767025513@163.com (S.C.); jxdky_xuzaide@126.com (Z.X.)

[2] School of Electrical and Automation Engineering, East China Jiaotong University, Nanchang 330013, China; y18907012925@163.com

* Correspondence: hanj947@163.com

Abstract

To address voltage fluctuations, low renewable energy permeability, and high power loss in low-voltage distribution networks (LVDNs) integrated with photovoltaic (PV) and energy storage systems (ESSs), a Chaotic Particle Swarm Optimization (PSO)-based hierarchical optimal operation method is proposed. Firstly, the mathematical model for grid-forming control (GFM)-based PV and ESSs in LVDNs is developed. Then, the multi-objective optimization problem is formulated to: (1) minimize voltage deviation, (2) maximize PV generation power, and (3) minimize power losses. Next, the objectives are ranked based on priority, and the multi-objective optimization problem is split into several single-objective sub-problems, each solved with the chaotic PSO algorithm. Several test studies confirm that the proposed strategy achieves faster convergence (68 iterations vs. 142, reducing total computation time by 36.9%), along with a marginal accuracy improvement over standard PSO. Finally, both simulation and hardware-in-the-loop (HIL) experimental results demonstrate the effectiveness and reliability of the proposed operation scheme in LVDNs.

Keywords: distribution networks; grid-forming; optimal operation; voltage quality

1. Introduction

The construction of a renewable energy source (RES)-dominated power system is essential for fulfilling climate commitments and accelerating the green energy transition [1,2]. Nevertheless, the high penetration of intermittent RESs, along with the proliferation of power electronic devices, poses new challenges to loads, active distribution networks (DNs), and the power system as a whole [3]. For example, the integration of numerous photovoltaic (PV) panels via grid-following (GFL) control-based converters can cause a voltage rise at the point of common coupling (PCC) and output power limitation in severe cases [4]. In response, the integration of inductive power–electronic loads results in a low power factor and harmonics at the PCC, thereby affecting system efficiency [5]. Due to the ability to support voltage and frequency, grid-forming control (GFM)-based converters have been increasingly applied in both the main grid and DNs [6,7]. Owing to the stable voltage-source characteristics, GFM-based converters offer better adaptability in low-voltage DNs (LVDNs) than GFL-based converters and present a novel perspective for tackling complex power quality (PQ) and RES utilization issues.

Check for updates

Academic Editors: Paulo Coelho and Mario Gomes

Received: 12 July 2026
Revised: 28 July 2026
Accepted: 31 July 2026
Published: 3 August 2026

Copyright: © 2026 by the authors. Licensee MDPI, Basel, Switzerland. This article is an open access article distributed under the terms and conditions of the Creative Commons Attribution (CC BY) license.

Existing research on GFM-based converters has primarily focused on control strategies. Due to the ability to provide inertia, damping, and frequency–voltage characteristics by simulating synchronous generators [8,9], droop control and virtual synchronous generator (VSG) control have been widely used. In recent years, nonlinear GFM schemes (including matching control and virtual oscillator control) have emerged as alternative approaches [10,11]. However, these GFM methods primarily focus on providing frequency and voltage support for the main grid. Consequently, the aforementioned GFM schemes neglect comprehensive PQ management in LVDNs, leading to fragmented research that targets individual issues rather than holistic optimization.

To address specific PQ problems in LVDNs, many GFM-based strategies have been proposed. In [12], an adaptive dynamic voltage support scheme for multiple GFM-based converters is proposed, which enables distributed, communication-free coordination through local parameter estimation to maximize voltage support efficiency. To mitigate harmonic distortion in weak grids, Tarraso et al. [13] proposed a selective harmonic compensation scheme for GFM-based converters, which uses virtual admittance branches to suppress specific harmonics and naturally shares the mitigation effort among parallel converters, effectively reducing THD at the PCC. Reactive power sharing among multiple GFM-based converters is another critical concern, since mismatches in line impedance or converter parameters may result in uneven power distribution and circulating currents. To address this issue, a feed-forward droop control with line impedance compensation is proposed in [14], which tracks line impedance online and compensates voltage drops in the dq frame. This approach effectively eliminates the adverse effects of impedance mismatches, achieving precise reactive power sharing and circulating current suppression without prior knowledge of line parameters. Beyond reactive power sharing, the adaptive droop control in [15] further addresses the trade-off between sharing accuracy and system damping by adjusting the reactive droop coefficient in real time, while remaining applicable to grids with unknown R/X ratios. However, most of the above studies adopt control-level strategies, which are insufficient for complex PQ issues.

In essence, this complex PQ and RES utilization issue constitutes a multi-objective optimization operation problem, which has been explored by some researchers from this perspective. In [16], a hybrid HGPC (combining Grey Wolf Optimization (GWO), Particle Swarm Optimization (PSO), and Cuckoo Search Optimization (CO))-based multi-objective approach is proposed for joint EV charging station and capacitor placement, balancing traffic flow capture, power loss, and voltage deviation in a DN. In [17], Nazih et al. employed a multi-objective whale optimization algorithm (WOA) to maximize distributed generator (DG) hosting capacity while reducing loss and voltage unbalance in unbalanced DNs. In [18], the Non-Dominated Sorting Genetic Algorithm II (NSGA-II) is adopted for multi-objective coordination of ESSs in DC DNs, effectively minimizing operational costs and energy losses. However, the Pareto-front nature of multi-objective optimization requires preference-based decision-making, which imposes a heavy computational burden and impedes real-time control for GFM-based converters.

To address voltage fluctuations, low RES permeability, and high power loss in LVDNs integrated with PV and ESSs, an improved PSO-based operation strategy is presented. The proposed strategy uses a priority-based hierarchical framework to convert the multi-objective problem into sequential single-objective ones for real-time implementation. Recently, various single-objective optimization algorithms have been developed for power system operational issues. For instance, Shaheen et al. [19,20] proposed a catch fish optimization algorithm (CFOA) and a circle search algorithm (CSA) for optimal power flow incorporating RES uncertainties. Meanwhile, Dimara et al. [21] introduced an evolutionary-based optimization approach for real-time PV error handling. In contrast, this study

employs a Lorenz-based chaotic PSO (C-PSO) [22] that dynamically adjusts acceleration coefficients to balance exploration and exploitation, achieving faster convergence and higher accuracy than conventional PSO. A comprehensive comparison of different algorithms is summarized in Table 1.

Table 1. Comparison of optimization algorithms.

Algorithm	Type	Key Mechanism	Pareto-Front Handling	Computational Cost
HGPC [16]	Multi-objective	Hybrid GWO-PSO-CS; dominance ranking	Yes	High
WOA [17]	Multi-objective	Spiral hunting; dominance ranking	Yes	High
NSGA-II [18]	Multi-objective	Non-dominated sorting; crowding distance	Yes	High
CFOA [19]	Single-objective	Fish schooling; hunting behavior	No	Moderate
CSA [20]	Single-objective	Circle-based geometric search	No	Moderate
GA [21]	Single-objective	Selection, crossover, mutation	No	Moderate
Proposed C-PSO	**Single-objective (hierarchical)**	**Lorenz chaos + dynamic tuning**	**No**	**Moderate–low**

The main contributions of this study are as follows:

(1) An optimal operation strategy is proposed for LVDNs integrated with GFM-based PV and ESSs, which coordinates PV and ESSs to reduce voltage deviation, maximize the power generation of the PV, and minimize losses.

(2) A hierarchical optimization idea-based multi-objective optimization algorithm is proposed, which splits the multi-objective problem into a sequence of single problems and facilitates real-time control applications. The order of priority is: (1) to minimize voltage deviation, (2) to maximize PV output power, and (3) to minimize power loss.

(3) An improved PSO algorithm is proposed for solving single-objective optimization problems. The proposed algorithm employs chaotic sequences generated from the Lorenz attractor rather than random numbers, enabling better initial value selection and faster solution speed.

2. Description and Models for GFM-Based PV and ESSs in LVDNs

2.1. System Description of LVDNs Integrated with GFM-Based PV and ESSs

Figure 1 shows the topology of a LVDN integrated with GFM-based PV and ESSs. The utility power grid supplies power to the LVDN through transmission lines and transformers. The PV panels and ESS are connected to a DC bus and linked to the utility power grid through a GFM-based converter. In addition, the GFM-based converter could also provide reactive power Q_{sl} to compensate the load reactive power demand, in order to maintain high-power-factor operation of the grid. The AC load is connected to the AC bus.

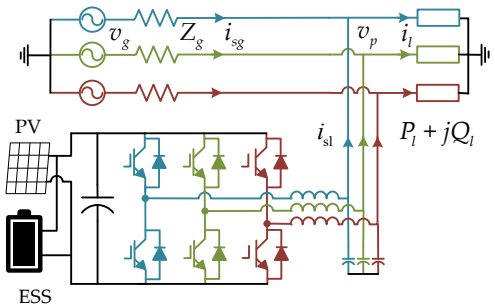

Figure 1. Topology of an LVDN integrated with GFM-based PV and ESS.

Based on the active power flow of the PV and ESS, the operation conditions can be divided into the following categories:

(a) The PV and ESS are disconnected, with $P_{pv} = P_{ba} = 0$ kW. The power grid supplies the load, and the converter provides reactive power compensation for the load.

(b) The ESS is disconnected, with $P_{ba} = 0$ kW. The power grid and PV panels supply the load, and the converter provides reactive power compensation for the load.

(c) The ESS is disconnected, with $P_{ba} = 0$ kW. The PV panels supply power to both the power grid and the load, while the converter provides reactive power for the load.

(d) The PV, ESS, and the power grid jointly supply the load, and the converter provides reactive power compensation for the load.

(e) The PV and ESS supply power for the power grid and load, and the converter provides reactive power compensation for the load.

(f) The power grid is disconnected: the PV and ESS jointly supply the load, and the converter provides reactive power compensation for the load.

The power flow under different conditions is presented in Figure 2. As illustrated, the integration of an ESS allows the PV panels to deliver surplus power to the power grid or store it in batteries for later deployment, thereby supporting peak shaving and valley filling while improving RES accommodation. Additionally, the coordinated operation between the ESS and GFM-based converters contributes to voltage quality enhancement and reactive power compensation.

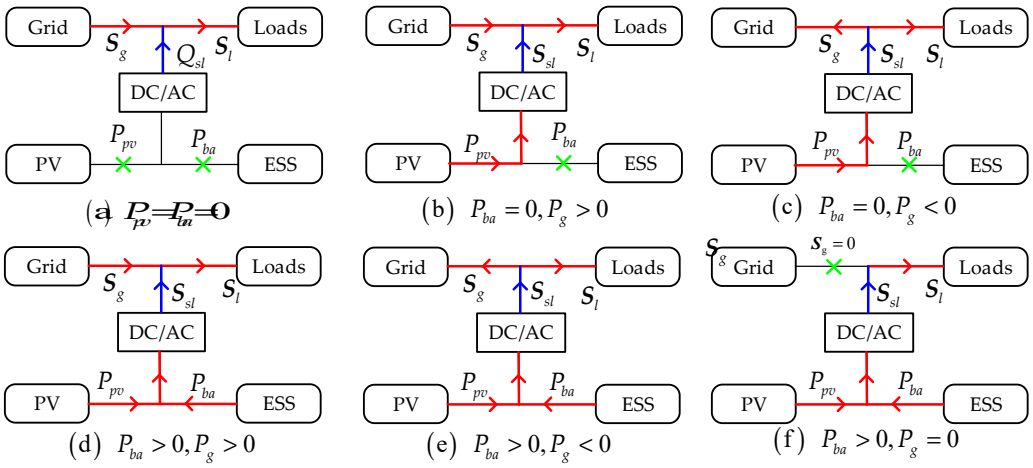

Figure 2. Power flow of the GFM-based PV and ESS.

2.2. Mathematical Model for GFM-Based PV and ESSs

Based on Figure 1, the load voltage can be described as:

$$\begin{bmatrix} v_{pd} \\ v_{pq} \end{bmatrix} = \begin{bmatrix} v_{gd} \\ v_{gq} \end{bmatrix} - \begin{bmatrix} R_g & -\omega L_g \\ \omega L_g & R_g \end{bmatrix} \begin{bmatrix} i_{sgd} \\ i_{sgq} \end{bmatrix} \tag{1}$$

The output currents of the GFM converter are expressed as:

$$\begin{bmatrix} i_{sld} \\ i_{slq} \end{bmatrix} = \begin{bmatrix} i_{ld} \\ i_{lq} \end{bmatrix} - \begin{bmatrix} i_{sgd} \\ i_{sgq} \end{bmatrix} \tag{2}$$

The complex power demand at the load terminal is:

$$S_l = 1.5\boldsymbol{v}_p \cdot \hat{\boldsymbol{i}}_l = 1.5\left(v_{pd} + jv_{pq}\right) \cdot \left(i_{ld} + ji_{lq}\right) = P_l + jQ_l \tag{3}$$

The load active and reactive power could be further described as:

$$\begin{bmatrix} P_l \\ Q_l \end{bmatrix} = 1.5 \begin{bmatrix} v_{pd} & v_{pq} \\ v_{pq} & -v_{pd} \end{bmatrix} \begin{bmatrix} i_{ld} \\ i_{lq} \end{bmatrix} \tag{4}$$

From Equations (1)–(3), the output complex power of the converter is derived as:

$$\boldsymbol{S}_{sl} = 1.5\boldsymbol{v}_p \cdot \hat{\boldsymbol{i}}_{sl} = P_{pv} + P_{ba} + jQ_{sl} \tag{5}$$

Based on Equation (5), the output apparent power of the converter can be written as:

$$|\boldsymbol{S}_{sl}| = \sqrt{\left(P_{pv} + P_{ba}\right)^2 + Q_{sl}^2} \tag{6}$$

The power supplied by the grid is expressed as:

$$\boldsymbol{S}_g = 1.5\boldsymbol{v}_g \cdot \hat{\boldsymbol{i}}_{sg} = P_g + jQ_g \tag{7}$$

Equation (7) can be further written as:

$$\begin{bmatrix} P_g \\ Q_g \end{bmatrix} = 1.5 \begin{bmatrix} v_{gd} & v_{gq} \\ v_{gq} & -v_{gd} \end{bmatrix} \begin{bmatrix} i_{sgd} \\ i_{sgq} \end{bmatrix} \tag{8}$$

According to the power balance theory, the complex power delivered by the grid is further expressed as:

$$\boldsymbol{S}_g = \boldsymbol{S}_l - \boldsymbol{S}_{sl} + 1.5\left(i_{sgd}^2 + i_{sgq}^2\right)\left(R_g + jX_g\right) \tag{9}$$

Since the phase-locked loop (PLL) tracks the phase angle of the grid voltage, $v_{gd} = kV_g^*$ and $v_{g\boldsymbol{q}} = 0$. Combing (8) and (9), Equation (9) can be rewritten as:

$$\begin{cases} P_g = 1.5kV_g^* i_{sgd} = \triangle P + 1.5MR_g \\ Q_g = -1.5kV_g^* i_{sgq} = \triangle Q + 1.5MX_g \end{cases} \tag{10}$$

where

$$\begin{cases} \Delta P = P_l - P_{pv} - P_{ba} \\ \Delta Q = Q_l - Q_{sl} \\ M = i_{sgd}^2 + i_{sgq}^2 \end{cases}$$

By squaring the two equations of Equation (10) individually and summing them, the following quadratic equation is obtained:

$$2.25\left|Z_g\right|^2 M^2 + \left[3\Omega - 2.25\left(kV_g^*\right)^2\right] M + \Delta P + \Delta Q = 0 \tag{11}$$

where $\left|Z_g\right|^2 = R_g^2 + X_g^2$ and $\Omega = \triangle PR_g + \triangle QX_g$.

Solving Equation (11), the following expression can be obtained:

$$M = \left\{1.5\left(kV_g^*\right)^2 - 2\Omega - \sqrt{\left[1.5\left(kV_g^*\right)^2 - 2\Omega\right]^2 - 4(\Delta P^2 + \Delta Q^2)\left|Z_g\right|^2}\right\} \Big/ \left(3\left|Z_g\right|^2\right) \tag{12}$$

Substituting Equation (12) into Equation (10), the grid current can be obtained as:

$$\begin{cases} i_{sgd} = \left(\Delta P + 1.5R_g M\right) / \left(1.5kV_g^*\right) \\ i_{sgq} = -\left(\Delta Q + 1.5\mathrm{X}_g M\right) / \left(1.5kV_g^*\right) \end{cases} \tag{13}$$

Moreover, by substituting Equation (13) into Equation (1) and performing algebraic manipulation, the magnitude of the PCC voltage can be calculated as:

$$\mathrm{V}_p = \sqrt{v_{pd}^2 + v_{pq}^2} = \sqrt{\left(kV_g^*\right)^2 + |Z_g|^2 M - 4\left[R_g\left(\triangle P + 1.5MR_g\right) + X_g\left(\triangle Q + 1.5MX_g\right)\right]/3} \quad (14)$$

Similarly, the system power loss is formulated as:

$$P_{loss} = 1.5I_{sg}^2 R_g = 1.5\left(i_{sgd}^2 + i_{sgq}^2\right)R_g = 1.5R_g M \quad (15)$$

2.3. Optimization Problem and Constraints

To improve the PQ and operational efficiency in LVDNs, the following three optimization objectives are primarily considered: (1) to minimize the voltage magnitude deviation; (2) to maximize the power generation of the PV; (3) to minimize the system power loss.

Therefore, the optimization objectives and constraints for the LVDNs integrated with the GFM-based PV and ESS can be described as follows:

$$Min\begin{cases} f_1 = \left(V_p - V_g^*\right)^2 \\ f_2 = \left(P_{pv} - P_{pv,max}\right)^2 \\ f_3 = P_{Loss}^2 \end{cases} \quad (16)$$

$$\text{s.}t.\begin{cases} |S_{sl}| \le |S_{sl}^*| \\ 0 \le P_{pv} \le P_{pv,max} \\ P_{ba,max}^- \le P_{ba} \le P_{ba,max}^+ \\ 0.90V_g^* \le V_p \le 1.07V_g^* \\ 0 \le I_{sl} \le I_{sl,max} \end{cases} \quad (17)$$

where (16) represents the optimization objective function, and (17) denotes the constraints, including converter capacity, output power of the PV and ESS, PCC voltage magnitude, converter output current, etc.

3. Simplified Multi-Objective Optimization Problem

The optimization problem described in (16) and (17) is inherently multi-objective in nature, meaning that its solution comprises a Pareto front rather than a unique optimum. Consequently, a preference-based selection step is required before the final decision can be implemented, and this step imposes a considerable additional computational cost. Thus, the multi-objective optimization problem in (16) and (17) is not easy to solve in real time.

To facilitate real-time implementation, this study proposes a hierarchical multi-objective optimization scheme that converts the original multi-objective problem in (16) and (17) into sequential single-objective ones according to the priority of each objective. The prioritization is established as follows: (1) the highest priority is given to minimizing voltage deviation, as secure and reliable voltage supply is the foremost guarantee for end-users; (2) the second priority is assigned to maximizing PV power generation, so that users can reap maximum economic benefits once voltage security is ensured; (3) the lowest priority is given to minimizing system power losses, as they are directly linked to operational costs. This hierarchical approach does not pursue global Pareto optimality but rather an engineering-feasible compromised optimum, where higher-priority objectives are strictly satisfied at the possible expense of lower-priority ones. This trade-off is intentional and justified by practical system requirements, where voltage security overrides economic considerations.

3.1. Operating Condition A

Under this condition, the first two optimization objectives could be accurately achieved, i.e., $V_P \in [0.9V_g^*, 1.07V_g^*]$ and $P_{pv} = P_{pv,max}$. Therefore, the optimization problem in (16) and (17) can be further written as:

$$Min\ f_3 = P_{Loss}^2 \tag{18}$$

$$\text{s.}t.\begin{cases} |S_{sl}| \le |S_{sl}^*| \\ P_{pv} = P_{pv,max} \\ P_{ba,max}^- \le P_{ba} \le P_{ba,max}^+ \\ 0.90V_g^* \le V_p \le 1.07V_g^* \\ 0 \le I_{sl} \le I_{sl,max} \end{cases} \tag{19}$$

3.2. Operating Condition B

Under this condition, only the first optimization objective can be accurately achieved, i.e., $V_P \in [0.9V_g^*, 1.07V_g^*]$. Therefore, the optimization problem in (16) and (17) can be further expressed as:

$$Min\ f_2 = \left(P_{pv} - P_{pv,max}\right)^2 \tag{20}$$

$$\text{s.}t.\begin{cases} |S_{sl}| \le |S_{sl}^*| \\ 0 \le P_{pv} \le P_{pv,max} \\ P_{ba,max}^- \le P_{ba} \le P_{ba,max}^+ \\ 0.90V_g^* \le V_p \le 1.07V_g^* \\ 0 \le I_{sl} \le I_{sl,max} \end{cases} \tag{21}$$

3.3. Operating Condition C

Under this condition, none of the optimization objectives can be accurately achieved. Thus, the optimization problem can be written as:

$$Min\ f_2 = \left(V_p - V_g^*\right)^2 \tag{22}$$

$$\text{s.}t.\begin{cases} |S_{sl}| \le |S_{sl}^*| \\ 0 \le P_{pv} \le P_{pv,max} \\ P_{ba,max}^- \le P_{ba} \le P_{ba,max}^+ \\ 0.80V_g^* \le V_p \le 1.20V_g^* \\ 0 \le I_{sl} \le I_{sl,max} \end{cases} \tag{23}$$

To maintain stable operation, the GFM-based converter should comply with stricter voltage constraints (e.g., 0.90–1.07 p.u.). Relaxing the voltage constraint to 0.80–1.20 p.u. enables feasible solutions under harsh conditions, avoiding operational failures.

Based on the proposed scheme, in Condition A, the optimization problem in (18) and (19) is first solved under the voltage constraint ($V_P \in [0.9V_g^*, 1.07V_g^*]$ and $P_{pv} = P_{pv,max}$). If a feasible solution exists, the system operates in its nominal high-efficiency mode. Otherwise, the algorithm proceeds to solve the relaxed sub-problem defined in Equations (20) and (21) for Condition B ($V_P \in [0.9V_g^*, 1.07V_g^*]$). Should Condition B also prove infeasible, the algorithm further degrades to Condition C. Thus, the multi-objective problem is transformed into three single-objective tasks, markedly accelerating the solution. An improved single-objective algorithm is then introduced in the next subsection to achieve faster and more accurate results.

4. Improved PSO-Based Algorithm for Single-Objective Optimization

4.1. Overview of Traditional PSO Algorithms

The PSO algorithm is a reliable population-based algorithm that generates an initial population at random. The particle movement of this population is updated at each iteration [16], and the update mode can be written as:

$$\begin{cases} V_i(m+1) = \eta V_i(m) + c_1 r_1 \left[p_{best,i}^m - X_i(m) \right] + c_2 r_2 \left[g_{best}^m - X_i(m) \right] \\ X_i(m+1) = X_i(m) + V_i(m+1) \end{cases} \tag{24}$$

where i $\in \{12, \ldots, |POP|\}$.

4.2. Improved PSO Algorithm

According to (24), the velocity update of traditional PSO particles relies on random numbers r_1 and r_2, which leads to slow convergence and difficulty in escaping local optima. To address this issue, an improved PSO is proposed, where all random numbers are replaced by chaotic sequences. The dynamic determinism and high sensitivity of chaotic systems effectively maintain population diversity and significantly enhance the convergence of random optimization methods. Specifically, the Lorenz attractor is used to generate chaotic sequences, which are then used for both initial particle generation and velocity updates in (24). The Lorenz attractor can be described as:

$$\begin{cases} d\alpha/dt = F_1(\alpha, \beta, \gamma) = \kappa(\beta - \alpha) \\ d\beta/dt = F_2(\alpha, \beta, \gamma) = \alpha(\lambda - \gamma) - \beta \\ d\gamma/dt = F_3(\alpha, \beta, \gamma) = \alpha\beta - \mu\gamma \end{cases} \tag{25}$$

If κ = 10, λ = 28, and μ = 8/3, respectively, the Lorenz system exhibits chaotic behavior. Equation (25) can be numerically solved by using the fourth-order Runge–Kutta (RK4) method. This method first fixes the initial conditions α_0, β_0, and γ_0 of the sequences $\{\alpha_m\}$, $\{\beta_m\}$, and $\{\gamma_m\}$, respectively. Then, the numerical values of $\{\alpha_m\}$, $\{\beta_m\}$, and $\{\gamma_m\}$ at time t_m can be calculated as:

$$\begin{cases} \alpha_m = \alpha_{m-1} + (n_{11} + 2n_{12} + 2n_{13} + n_{14})/6 \\ \beta_{\mathrm{m}} = \beta_{m-1} + (n_{21} + 2n_{22} + 2n_{23} + n_{24})/6 \\ \gamma_{\mathrm{m}} = \gamma_{m-1} + (n_{31} + 2n_{32} + 2n_{33} + n_{34})/6 \end{cases} \tag{26}$$

$$\begin{cases} n_{i1} = F_i(\alpha_{m-1}, \beta_{m-1}, \gamma_{m-1})\Delta t \\ n_{i2} = F_i(\alpha_{m-1} + n_{11}/2, \beta_{m-1} + n_{21}/2, \gamma_{m-1} + n_{31}/2)\Delta t \\ n_{i3} = F_i(\alpha_{m-1} + n_{12}/2, \beta_{m-1} + n_{22}/2, \gamma_{m-1} + n_{32}/2)\Delta t \\ n_{i4} = F_i(\alpha_{m-1} + n_{13}/2, \beta_{m-1} + n_{23}/2, \gamma_{m-1} + n_{33}/2)\Delta t \end{cases} \tag{27}$$

where $m = 1, 2, \ldots, M$ and $t_m = t_{m-1} + \Delta t$.

To keep the values of sequences $\{\alpha_m\}$, $\{\beta_m\}$, and $\{\gamma_m\}$ within the interval [0, 1], these sequences must be normalized as follows:

$$\hat{\iota}_m = \frac{\iota_m - \iota_m^{min}}{\iota_m^{max} - \iota_m^{min}} \tag{28}$$

where $\iota \in \{\alpha, \beta, \gamma\}$.

The chaotic sequence $\{\alpha_m\}$ corresponding to the state variable α is used to generate the initial population. Therefore, for a D-dimensional problem, the size of the chaotic

sequence must satisfy $K \geq D|POP|$. The matrix Γ corresponding to the sequence $\{\alpha_m\}$ can be defined as:

$$\Gamma = \begin{bmatrix} \alpha_1 & \cdots & \alpha_D \\ \vdots & \ddots & \vdots \\ \alpha_{D(|POP|-1)} & \cdots & \alpha_{D|POP|} \end{bmatrix} \tag{29}$$

Thus, the initial population can be generated as follows:

$$\Gamma_{ij} = \Gamma_{j,min} + (\Gamma_{j,max} - \Gamma_{j,min})\Gamma_{ij} \tag{30}$$

where $j = 1, 2, \ldots, D$.

To update the velocity described in (24), the chaotic sequences $\{\beta_m\}$ and $\{\gamma_m\}$ are used to replace the random numbers r_1 and r_2. The matrices corresponding to the sequences $\{\beta_m\}$ and $\{\gamma_m\}$ can be written as:

$$\begin{cases} \Delta = \begin{bmatrix} \beta_1 & \cdots & \beta_{|\mathrm{POP}|} \\ \vdots & \ddots & \vdots \\ \beta_{|\mathrm{POP}|(\mathrm{T}^{max}-1)} & \cdots & \beta_{\mathrm{T}^{max}|\mathrm{POP}|} \end{bmatrix} \\ \Theta = \begin{bmatrix} \gamma_1 & \cdots & \gamma_{|\mathrm{POP}|} \\ \vdots & \ddots & \vdots \\ \gamma_{|\mathrm{POP}|(T^{max}-1)} & \cdots & \gamma_{\mathrm{T}^{max}|\mathrm{POP}|} \end{bmatrix} \end{cases} \tag{31}$$

Then, at each iteration m, for each particle i, the values of r_1 and r_2 are extracted from matrices Δ and Θ as follows:

$$\begin{cases} r_1 = \Delta_{mi} \\ r_2 = \Theta_{mi} \end{cases} \tag{32}$$

Therefore, the updated velocity is then modified as:

$$\begin{cases} V_i(m+1) = \eta V_i(m) + c_1\Delta_{mi}\left[p^m_{best,i} - X_i(m)\right] + c_2\Theta_{mi}\left[g^m_{best} - X_i(m)\right] \\ X_i(m+1) = X_i(m) + V_i(m+1) \end{cases} \tag{33}$$

where $m = 1, 2, \ldots, T^{max}$.

The flowchart of the improved PSO-based optimal operation strategy for GFM-based PV and ESSs is shown in Figure 3. To align with GFM-based LVDNs' operational demands, the proposed chaotic PSO incorporates three key adaptations: Lorenz-attractor-generated chaotic sequences are adopted to initialize the population of the PSO; initial particles are constrained to the physically feasible region of LVDNs to eliminate infeasible solutions that may disrupt system operation; core control variables (P_{ba}, Q_{sl}, and P_{pv}) and priority objectives (voltage deviation minimization, PV generation maximization, and system power loss reduction) of GFM converters are embedded into the algorithm. In the proposed scheme, the constraints in Equation (16) are handled via a penalty function method combined with a constraint repair strategy. The fitness function augments the original objective with penalty terms for each violation, using dynamically increasing penalty coefficients to allow initial exploration and later enforce feasibility.

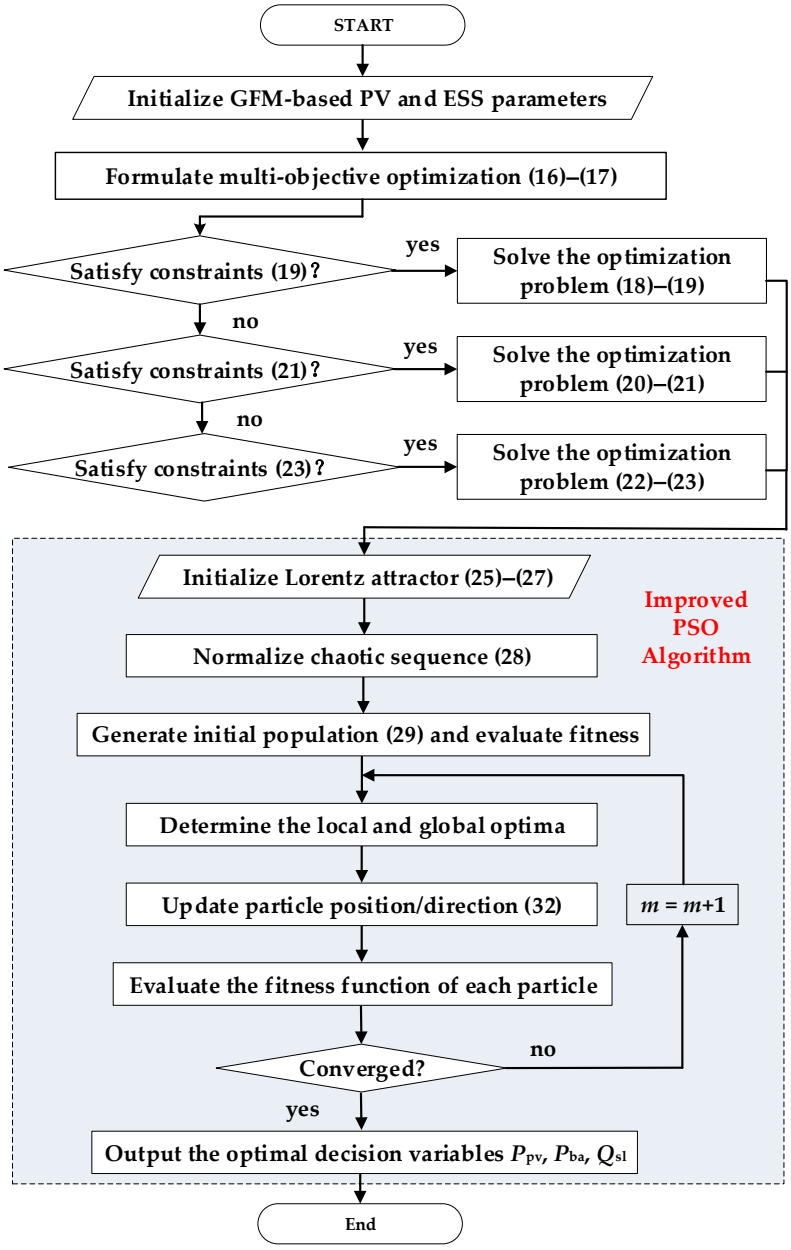

Figure 3. Flowchart of the optimal operation strategy.

5. Simulation Verification

This section validates the effectiveness and rationality of the proposed optimal operation strategy in the simulations. The electrical and control parameters used in the simulations are shown as Table 2. In addition, the GFM-based converter adopts droop control.

Furthermore, the parameters of the proposed PSO are selected within commonly used ranges, with their specific values determined through offline tests. The Lorenz system adopts its classical parameters, striking a balance between preserving chaotic dynamics and computational efficiency. The normalization strategy employs linear mapping to unify all decision variables to the same order of magnitude, thereby preventing any single dimension from dominating the particle update process.

Table 2. Parameters used in the verification.

	Symbol	Value
Electrical parameters	V_g^*	311 V
	ω	314 rad/s
	Z_g	2 + j0.016 Ω
	S_l	10 + j10 kVA
	$\lvert S_{sl}^* \rvert \lvert S_{sl}^* \rvert$	8 kVA
	$I_{sl,max}$	50 A
	$P_{ba,max}^+$	4 kW
	$P_{ba,max}^-$	−4 kW
Parameters of proposed PSO	η	0.6
	Δt	0.05
	κ	10
	λ	28
	μ	8/3
	$\lvert POP \rvert$	30
	M	300
Control parameters	D_m	3.14×10^{-4} rad/(s·W)
	D_n	1.9×10^{-3} V/var
	k_{vp}, k_{vi}	1, 100
	k_{ip}, k_{ii}	6, 0.01

5.1. Performance Analysis of the Improved PSO Algorithm

To verify the practicality and robustness of the proposed scheme, several studies were conducted on a platform with an Intel Core i5-12600KF CPU, 32 GB of RAM, and MATLAB R2024a. In addition, the optimization problem is solved using parallel computing techniques. In this subsection, the maximum PV output power is 4 kW, and the grid voltage amplitude is 1 p.u.

5.1.1. Comparative Analysis with Other Algorithms

In this case, thirty independent trials were performed for each algorithm under identical settings. By calculation with the proposed and other algorithms (including traditional PSO, the GA, and the Free Energy Perturbation (FEP) algorithm), the system operates in Operating Condition A, where the PCC voltage remains within acceptable limits, and the PV output power is 4 kW. The power loss is approximately 0.5950 kW.

Figure 4 demonstrates that the proposed algorithm yields the highest accuracy and fastest convergence. By integrating the Lorenz chaotic map for deterministic velocity updates, the algorithm effectively preserves population diversity and rapidly escapes local optima.

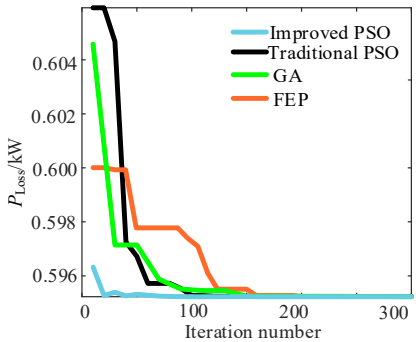

Figure 4. Power loss with different algorithms under $P_{pv,max}$ = 4 kW.

5.1.2. Computational Cost Comparison

It can be observed from Table 3 that the average per-iteration time of the proposed algorithm is 0.81 µs, which is 30.6% longer than that of traditional PSO (0.62 µs). This increase is a reasonable trade-off caused by the computational overhead of generating Lorenz-based chaotic sequences instead of simple uniform random numbers. Yet C-PSO cuts average convergence iterations by 52.1% (142 to 68), thanks to normalized chaotic sequences ([0.1, 0.9]) that avoid extreme particle positions and boost global search efficiency. This iteration reduction offsets per-iteration overhead, slashing the total convergence time by 36.9% (55.1 µs vs. 87.3 µs). This improvement shows strong potential for supporting real-time control requirements. Notably, C-PSO retains better optimization accuracy and a smaller standard deviation, helping to maintain solution quality alongside efficiency gains.

Table 3. Comparative analysis of computational cost.

Algorithm	Convergence Iterations	Avg. Time per Iteration (µs)	Avg. Total Convergence Time (µs)	P_{Loss} (kW)	Std. Deviation
Traditional PSO	142 ± 11	0.62 ± 0.03	87.3 ± 4.2	0.5953	1.68×10^{-4}
Chaotic PSO	68 ± 7	0.81 ± 0.04	55.1 ± 3.5	0.5950	8.56×10^{-8}

5.1.3. Convergence Characteristics of C-PSO with Various Parameters

To further test the sensitivity of key parameters (including the inertia weight (η) and chaotic map time step (Δt)) for the proposed algorithm, several studies are implemented.

As seen in Figure 5a and Table 4, the inertia weight η = 0.6 achieves the best overall performance, characterized by the minimum optimal P_{Loss}, smallest standard deviation, and fastest convergence. A smaller η (0.4) weakens global search capability, leading to slower convergence, while a larger η (1.0) reduces local search precision, resulting in sub-optimal solutions and higher standard deviations. This confirms that an intermediate inertia weight balances global exploration and local exploitation.

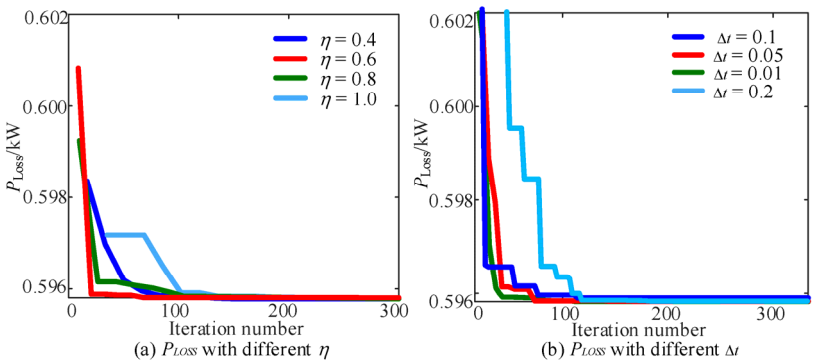

Figure 5. Convergence characteristics of the proposed algorithm with various parameters.

Table 4. Comparative analysis with different inertia weights.

η	Optimal P_{Loss} (kW)	Average Value (kW)	Standard Deviation	Convergence Iterations
0.4	0.5951	0.5953	1.21×10^{-7}	98 ± 9
0.6	0.5950	0.5953	8.56×10^{-8}	68 ± 7
0.8	0.5951	0.5953	1.53×10^{-7}	95 ± 10
1.0	0.5954	0.5956	3.27×10^{-7}	123 ± 14

From Figure 5b and Table 5, a time step smaller than 0.05 increases computational overhead due to the need for more RK4 steps to generate chaotic sequences, without significant performance gains, while a time step larger than 0.1 reduces chaotic sequence diversity (lower entropy), leading to premature convergence and worse optimal values. The original setting $\Delta t = 0.05$ is close to the optimal range, yielding performance comparable to $\Delta t = 0.01$.

Table 5. Comparative analysis of chaotic map time step.

Δt	Optimal P_{Loss} (kW)	Average Runtime (μs)	Convergence Iterations
0.01	0.5950	90.0 ± 5.1	65 ± 7
0.05	0.5950	55.1 ± 3.5	68 ± 7
0.1	0.5951	65.1 ± 4.5	93 ± 9
0.2	0.5952	72.0 ± 3.2	131 ± 12

5.1.4. Performance Comparison with Different Chaotic Maps

To verify the rationality of selecting the Lorenz attractor, this subsection compares the proposed algorithm with two common chaotic maps (Tent and Logistic) and traditional PSO.

In this test study, the Lorenz attractor (original) uses parameters $\sigma = 10$, $\rho = 28$, and $\beta = 8/3$ (solved via RK4), the Tent map follows $x_{n+1} = 2x_n$ (initial value $x_0 = 0.3$), and the Logistic map uses $x_{n+1} = 3.9x_n(1 - x_n)$ (initial value $x_0 = 0.4$). Evaluation metrics include optimal P_{Loss}, standard deviation, convergence iterations, and average convergence time, with each algorithm running 30 independent trials to ensure reliability.

The results presented in Figure 6 and Table 6 demonstrate that all chaotic PSO variants outperform traditional PSO in both accuracy and convergence speed. The Lorenz-based C-PSO achieves the highest accuracy (optimal $P_{Loss} = 0.5950$ kW, standard deviation $= 8.56 \times 10^{-8}$), attributed to the high-dimensional chaotic sequence that provides richer population diversity. The Tent-based C-PSO exhibits the shortest convergence time (52.5 μs) due to its one-dimensional structure and no requirement for RK4 numerical solutions, making it suitable for resource-constrained embedded systems. The Logistic-based C-PSO performs moderately in both accuracy and efficiency. These results confirm the rationality of selecting the Lorenz attractor for the proposed strategy, as it balances high accuracy and practical feasibility.

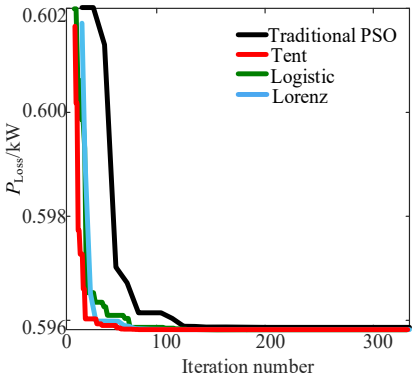

Figure 6. Convergence characteristics of the proposed algorithm with different chaotic maps.

Table 6. Performance comparison of different chaotic maps.

Algorithm	Optimal P_{Loss} (kW)	Std. Deviation	Convergence Iterations	Avg. Convergence Time (μs)
Traditional PSO	0.5953	1.68×10^{-4}	142 ± 11	87.3 ± 5.2
Chaotic PSO (Lorenz)	0.5950	8.56×10^{-8}	68 ± 7	55.1 ± 3.5
Chaotic PSO (Tent)	0.5951	1.12×10^{-4}	60 ± 9	52.5 ± 4.2
Chaotic PSO (Logistic)	0.5951	1.35×10^{-4}	65 ± 10	53.8 ± 4.8

5.2. Test Study Analysis

To further verify the correctness of the proposed strategy, the simulation model is established in the MATLAB/Simulink platform. The GFM-based converter adopts the traditional P-ω/Q-V droop control, while the PV and ESS units are governed by PI controllers on the DC side. Table 7 presents the optimal operation results with different $P_{pv,\max}$. In addition, to deeply analyze the optimal operation, several test studies are implemented: in test study 1, the PV is disconnected; in test study 2, the maximum output power of PV is 6 kW; in test study 3, the off-grid transitions are implemented.

Table 7. Performance comparison under various operation conditions.

			k = 0.9	1	1.1	1.2
1	$P_{pv,max}$ = 0 W	V_L (V)	\	280.63	315.41	332.77
		P_{ba} (kW)	\	4.00	4.00	0.42
		Q_{sl} (kvar)	\	6.93	6.93	7.99
		P_{Loss} (kW)	\	0.76	0.60	1.14
2	$P_{pv,max}$ = 4 kW	V_L (V)	262.70	289.74	323.34	332.77
		P_{pv} (kW)	4.00	4.00	4.00	4.00
		P_{ba} (kW)	3.76	1.77	1.76	−3.49
		Q_{sl} (kvar)	1.96	5.54	5.55	6.18
		P_{Loss} (kW)	1.32	0.60	0.48	1.25
3	$P_{pv,max}$ = 6 kW	V_L (V)	262.49	290.25	324.66	332.78
		P_{pv} (kW)	6.00	6.00	6.00	6.00
		P_{ba} (kW)	1.53	−0.12	0.08	−3.94
		Q_{sl} (kvar)	2.70	5.42	5.19	−3.49
		P_{Loss} (kW)	1.13	0.60	0.48	2.87

Furthermore, the improved PSO algorithm is not executed in every control cycle; instead, it is activated only upon the occurrence of significant disturbances, such as grid voltage fluctuations, load changes, or variations in PV output.

5.2.1. Test Study 1

In test study 1, the PV panel is disconnected, and only the ESS is connected.

Figures 7 and 8 present the waveforms of grid voltage, PCC voltage, grid current, and active/reactive power. As shown in Figures 7 and 8 and Table 5, within [0.1, 0.3] s, the grid voltage amplitude is 1.0 p.u., and the optimized PCC voltage is 280.63 V. Concurrently, the ESS discharges at its maximum power of 4 kW, and the reactive power generated by the converter is 6.93 kvar. In this condition, the system operates in Condition C, which means that the two optimization objectives—minimizing line loss and PCC voltage deviation—cannot be fully achieved.

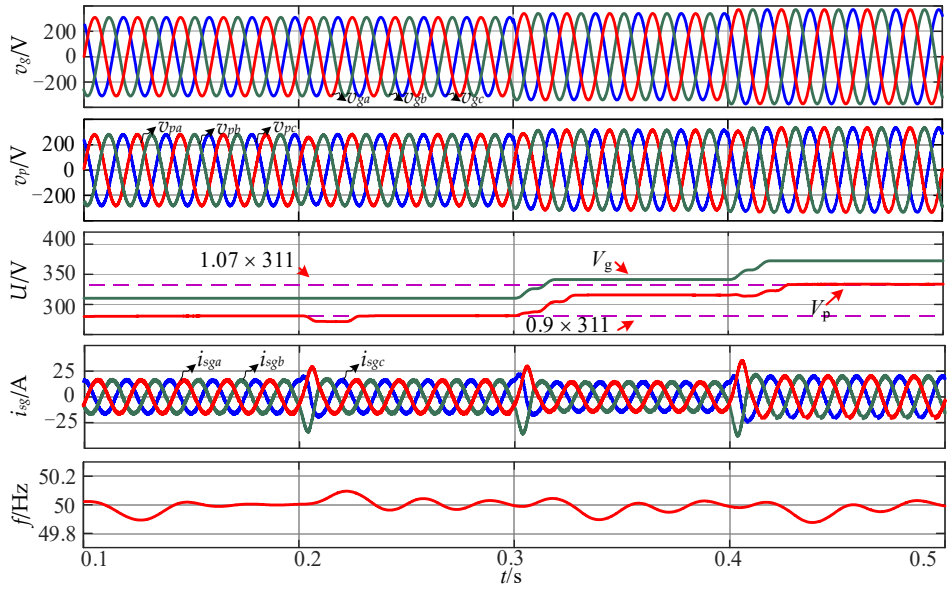

Figure 7. Waveforms of voltage, current, and frequency in case 1.

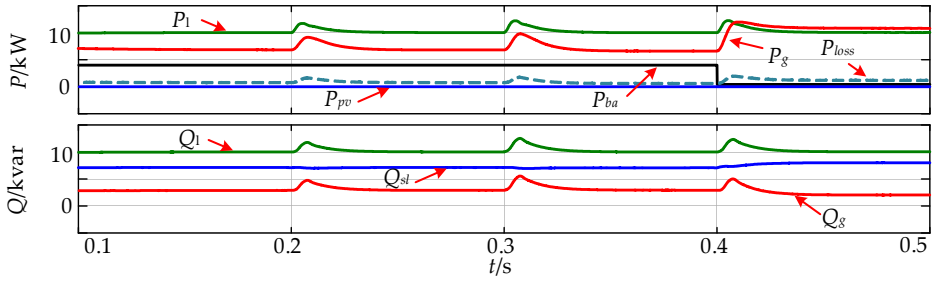

Figure 8. Power waveforms in test study 1.

Within [0.3, 0.5] s, the grid voltage rises to 1.1 and 1.2 p.u. To offset the over-voltage, the GFM-based converter dynamically adjusts reactive power absorption and curtails the output active power of the ESS. Consequently, the PCC voltage is safely maintained at 315.41 V and 332.77 V (<1.07 p.u.). Specifically, within the [0.4, 0.5] s interval, when the grid voltage amplitude is 373.35 V (1.2 p.u.), the optimized ESS discharge power is 0.42 kW and Q_{sl} is 7.99 kvar. The system still operates under Condition A, with the PCC voltage deviation strictly within the allowable range and a minimum line loss of 2.88 kW.

Furthermore, the system frequency remains strictly within the permissible 49.8–50.2 Hz range. Concurrently, the chaotic PSO algorithm minimizes line losses by rapidly optimizing the P_{ba}-Q_{sl} combination. In response to grid voltage variations (1.0–1.2 p.u.), the GFM-based converter dynamically adjusts Q_{sl} to compensate for line impedance drops, successfully maintaining the PCC voltage within the allowable limits.

5.2.2. Test Study 2

In this test study, the PV panel and ESS are connected, and $P_{pv,max}$ = 6 kW.

As presented in Figures 9 and 10 and Table 7, within [0.1, 0.3] s, the system coordinates PV and ESS outputs under varying grid voltages. When the grid sags to 280.01 V (0.9 p.u.), the ESS shifts to discharging mode (1.53 kW) to supplement the maximum PV generation, compensating for the energy deficit. Conversely, when the grid recovers to 311.13 V (1.0 p.u.), the ESS dynamically switches to charging mode (0.12 kW) to absorb excess energy. This demonstrates how the strategy utilizes the ESS as a buffer to balance power flow and stabilize the PCC voltage. Within [0.3, 0.4] s and [0.4, 0.5] s, the grid voltage rises to 342.24 V (1.1 p.u.) and 373.35 V (1.2 p.u.), respectively. Under the proposed scheme, the PCC voltage

is successfully maintained within [0.90 p.u., 1.07 p.u.]. Consequently, the system operates under Condition A (where voltage and frequency are strictly regulated, PV operates at maximum power, and the ESS charges). These results align with Table 7, confirming the effectiveness of the proposed strategy.

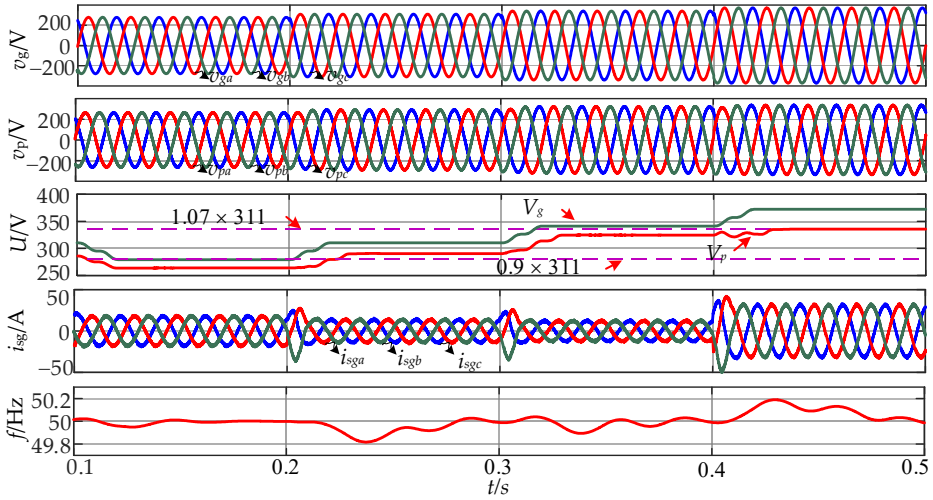

Figure 9. Waveforms of voltage, current, and frequency in test study 2.

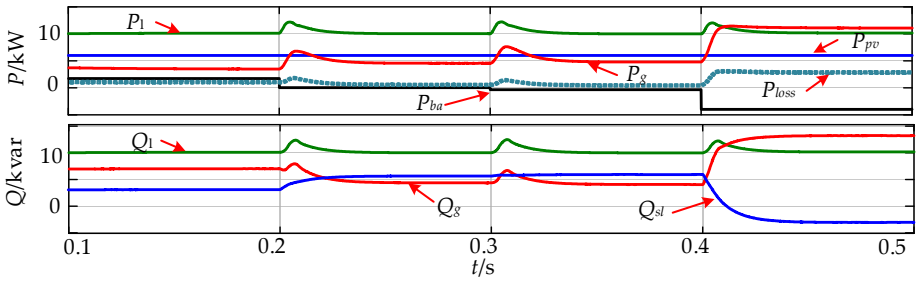

Figure 10. Power waveforms in test study 2.

5.2.3. Test Study 3

In this test, the PV panel and ESS are connected to the converter, and $P_{pv,max}$ = 4 kW, where the system switches from grid-connected to off-grid mode at 0.3 s.

According to Figures 11 and 12 and Table 7, within [0.1, 0.3] s (grid-connected), the grid voltage is 373.35 V (1.2 p.u.); after optimization, the magnitude of PCC voltage is 332.77 V, the PV panel operates at maximum power, the ESS charges at 3.49 kW, the reactive power generated by the converter is 6.18 kvar, and the system operates under Condition A. The grid is disconnected at 0.3 s, and the system transitions to off-grid mode. As shown in Figure 10, the GFL-based converter relies entirely on a PLL; upon grid disconnection, it loses its tracking target, causing severe voltage distortion and frequency oscillations. Unlike the GFL baseline, the proposed GFM strategy leverages its voltage-source characteristics to autonomously establish the grid frequency and a stable PCC voltage without severe transients (as seen in Figure 11). Within 0.03 s, the PCC voltage strictly stabilizes at 311.13 V (1 p.u.), and the frequency remains within 49.8–50.2 Hz. Simultaneously, the local load demand is fully satisfied by the coordinated PV and ESS output, demonstrating highly reliable off-grid performance.

The simulation results for the three cases are consistent with the optimized operation in Table 7, further confirming the effectiveness of the proposed optimization scheme.

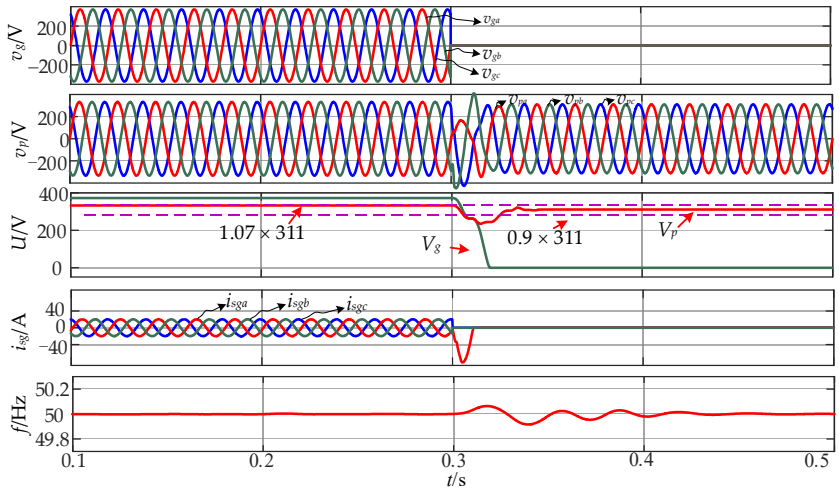

Figure 11. Simulation waveforms with the GFM scheme in test study 3.

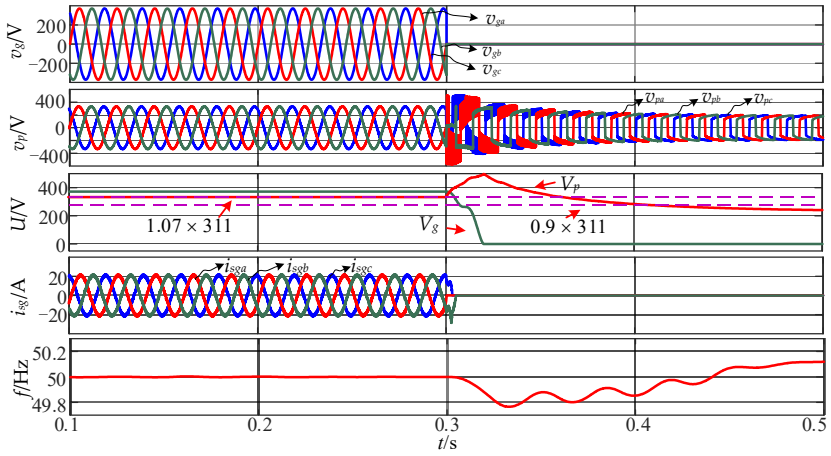

Figure 12. Simulation waveforms with the GFL scheme in test study 3.

5.3. Comparative Analysis of the Test Study Results

In this subsection, the effectiveness of the proposed scheme is further verified by testing another two schemes, including only injecting active power (IAP) and only injecting reactive power (IRP).

To evaluate the performance of proposed scheme, the voltage deviation is defined as:

$$\Delta V_p = \left| V_p - V_g^* \right| / V_g^* \tag{34}$$

Figure 13a–f show the comparison of optimization results under three schemes. As can be seen, the proposed optimization scheme demonstrates superior performance over the IAP and IRP schemes in most cases. For example, as illustrated in Figure 13a, when the grid voltage is 1.0 p.u., the proposed scheme achieves a minimum voltage deviation of 0.092 p.u., outperforming the IAP (0.106 p.u.) and IRP (0.167 p.u.) schemes. When the grid voltage reaches 1.1 p.u. (Figure 13d), while all schemes satisfy the voltage constraints, the proposed strategy achieves a remarkably lower power loss of 0.48 kW, compared to 1.51 kW (IAP) and 1.85 kW (IRP). Analytically, both the IAP and IRP schemes are forced to inject excessive currents to meet voltage limits, inherently increasing thermal losses on distribution lines. By contrast, the proposed multi-objective approach strategically balances the output vectors, eliminating unnecessary circulating currents and optimizing overall energy transfer efficiency.

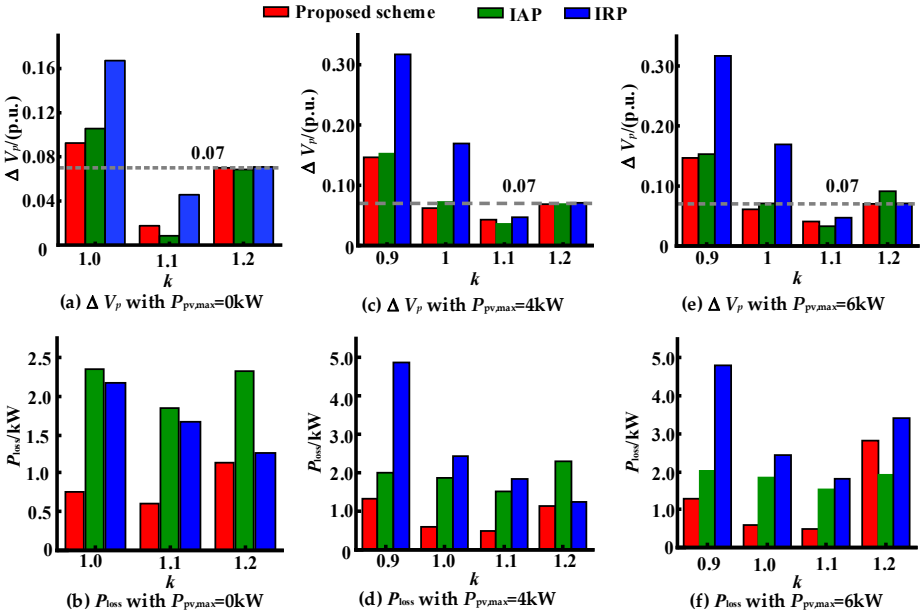

Figure 13. The optimization results under various schemes.

6. Controller Hardware-in-the-Loop Experimental Validation

To validate the real-time execution capability of the proposed strategy, a Controller Hardware-in-the-Loop (CHIL) platform is established, as shown in Figure 14. The LVDN physical power stage is emulated in the Modelingtech MT 6090 simulator, manufactured by Shanghai Yuankuan Energy Technology Co., Ltd. (Shanghai, China), with a 1μs time step for high-fidelity transient reproduction. The control sampling period and the PWM switching frequency are both set to 10 kHz (i.e., 100 μs). By calculation, the worst-case execution time of the underlying GFM control loop—including measurement, communication, and controller update—is estimated to be approximately 85 μs, which is well within the 100 μs control interval, leaving a 15 μs safety margin. It should be noted that the PSO optimization is not executed in every control cycle; it is triggered only upon significant disturbances (grid voltage fluctuations, load changes, or PV variations). The measured execution time for a full PSO optimization is approximately 20 ms, which is acceptable for disturbance-response scenarios, as typical grid disturbances evolve on a time scale of hundreds of milliseconds to seconds. In steady-state operation, the system relies on previously computed optimal set-points to avoid unnecessary computational overhead. For future hardware implementation, we plan to adopt FPGA-based acceleration to further reduce the PSO computation latency and enhance overall real-time performance.

Figures 15 and 16 present the dynamic responses under grid-connected conditions. Both test study 1 and 2 in simulation are conducted in the CHIL experimental setup.

As shown in Figures 15 and 16, the real-time oscilloscope performs the waveforms of the PCC voltage (v_p), grid voltage (v_g), load current (i_l), and grid current (i_{sg}). As can be seen, the waveforms confirm that the proposed optimal operation scheme could accurately execute the multidimensional optimal set-points in real time. Even during the step fluctuations of v_g (0.9 p.u. to 1.2 p.u.), the GFM converter dynamically compensates for the reactive power, maintaining v_p strictly within the safe limits without severe transient overshoots.

To explicitly evaluate the transient robustness, comparative real-time experiments were conducted at the exact instant of grid disconnection. As illustrated in Figure 17, despite the 25 μs hardware control delay, the proposed GFM strategy seamlessly transitions to off-grid mode, autonomously establishing a highly stable sinusoidal v_p profile within 0.03 s. In stark contrast, as demonstrated in Figure 18, the traditional GFL baseline completely

loses its tracking target upon grid disconnection, leading to immediate and severe PCC voltage distortion. These real-time CHIL results perfectly align with the theoretical analysis and offline simulations, firmly substantiating the computational efficiency and practical reliability of the proposed strategy in LVDNs.

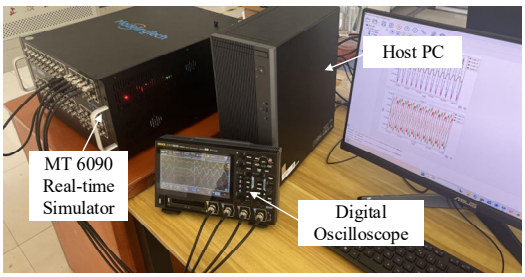

Figure 14. CHIL experimental setup.

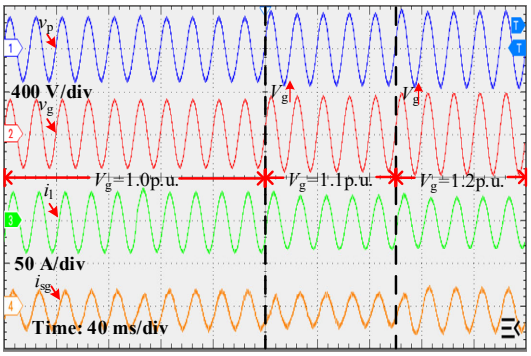

Figure 15. Experimental waveforms under test study 1.

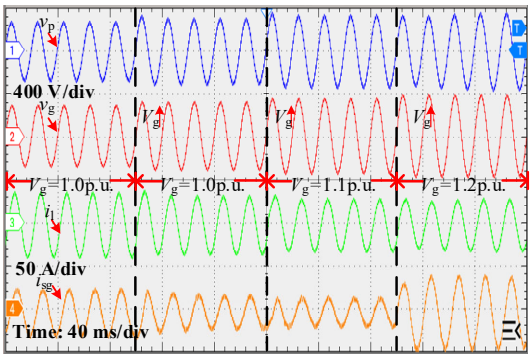

Figure 16. Experimental waveforms under test study 2.

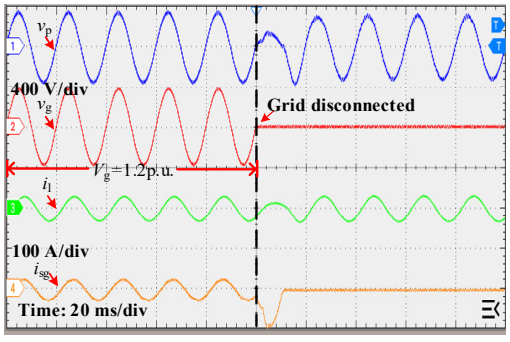

Figure 17. Real-time GFM waveforms during the transition.

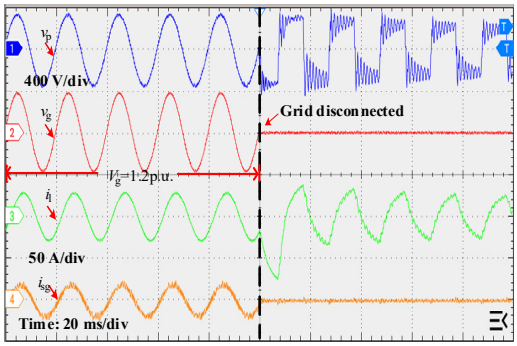

Figure 18. Real-time GFL waveforms during the transition.

7. Conclusions

In this study, an improved PSO-algorithm-based hierarchical optimal operation strategy is proposed for LVDNs integrated with GFM-based PV and ESSs. The proposed strategy can simultaneously address voltage fluctuations, low penetration of RES, and high system power losses, and it is convenient for real-time implementation. The main conclusions are as follows:

(1) A priority-based hierarchical simplification method is designed to enable real-time control feasibility, which transforms the multi-objective optimization problem into single ones. The comparative analysis of optimization results verifies the effectiveness of the proposed optimization strategy in reducing load voltage deviation and system power losses.

(2) Compared with traditional algorithms (NSGA-II, GA, and PSO), the improved PSO algorithm exhibits better performance: reducing total convergence time by 36.9% while achieving an optimal power loss of 0.5950 kW.

(3) The proposed strategy is verified to support reliable operation in both grid-connected and off-grid modes, maintaining the PCC voltage within 0.90–1.07 p.u. and frequency within 49.8–50.2 Hz under all test conditions.

Future work will extend the proposed strategy to multi-GFM-based converters in parallel operation, refine the system loss model, and develop high-dimensional optimization methods for complex LVDNs to address scalability challenges in coordinating multiple DGs. Meanwhile, robust optimization will be employed to enhance anti-interference capability, ultimately improving the strategy's engineering practicality and scalability in large-scale networks.

Author Contributions: Conceptualization, X.Z., J.H., B.C. and Z.X.; methodology, X.Z., B.C. and Z.Y.; software, S.W. and S.C.; validation, S.W. and S.C.; formal analysis, J.H.; investigation, J.H., S.W. and S.C.; resources, Z.X.; data curation, B.C., S.W. and S.C.; writing—original draft preparation, Z.Y.; writing—review and editing, Z.Y. and X.Z.; visualization, Z.Y.; supervision, Z.X.; project administration, Z.X.; funding acquisition, X.Z. All authors have read and agreed to the published version of the manuscript.

Funding: This research was funded by the State Grid Jiangxi Electric Power Co., Ltd., Science and Technology Project under Grant 52182026000G.

Data Availability Statement: The original contributions presented in this study are included in the article. Further inquiries can be directed to the corresponding author.

Conflicts of Interest: Authors X.Z., B.C., S.W., S.C. and Z.X. were employed by the State Grid Jiangxi Electric Power Research Institute. The remaining authors declare that the research was conducted in the absence of any commercial or financial relationships that could be construed as a potential conflict of interest. The funder was involved in the study design, the writing of this article, and the decision to submit it for publication.

Nomenclature

P_{pv}, P_{ba}	Output power of the PV panel and energy storage system (ESS)
Q_{sl}	Output reactive power of the converter
Z_g, R_g, L_g	Equivalent impedance, resistance and reactance of the power grid
$\boldsymbol{v}_p$, $\boldsymbol{v}_g$	Point of common coupling (PCC) voltage and grid voltage vectors
$\boldsymbol{i}_l$, $\boldsymbol{i}_{sg}$	Load current and grid current vectors
v_{pd}, v_{pq}	Dq axis voltages at PCC
i_{sgd}, i_{sgq}	Dq-axis components of grid current
v_{gd}, v_{gq}	Dq-axis components of grid voltage
i_{sld}, i_{slq}	Dq-axis components of the converter output current
i_{ld}, i_{lq}	Dq-axis components of the load current
V_p, V_g	Magnitudes of the PCC voltage and grid voltage
I_{sg}, I_{sl}	Magnitudes of grid current and converter current
S_g, S_l, S_{sl}	Complex power of the power grid, load and converter
P_g, Q_g	Active and reactive power generated by the power grid
P_l, Q_l	Load active and reactive power
P_{sl}, Q_{sl}	Active and reactive power delivered by the converter
ΔV_p	Voltage deviation at PCC
*	Nominal quantities
k	Voltage ratio between nominal voltage and actual voltage
ˆ	Conjugate quantities
max, min	Maximum and minimum quantities
+, −	Discharging and charging power of the ESS
| |	Magnitude of complex variables
P_{loss}	System loss
$X_i(m)$, $V_i(m)$	Position and velocity of the i-th particle
$\|POP\|$, M	Maximum population size and iterations number
c_1, c_2	Acceleration coefficients
η, r_1 and r_2	Inertia coefficient, random values
$p^m_{best,i}$	Optimal position achieved by the i-th particle at the m-th iteration.
g^m_{best}	Current global optimal position, i.e., the optimal solution
α, β, γ	State variables of the Lorenz system
κ, λ, μ	System parameters
Δt	Time step
Γ, Δ, Θ	Parameter matrices
Γ_{ij}	Value of the j-th decision variable of the i-th particle
D_m, D_n	*P-f* and *Q-V* droop coefficient
k_{vp}, k_{vi}	Proportional and integral gains of the voltage outer loop
k_{ip}, k_{ii}	Proportional and integral gains of the current inner loop

References

1. Xiong, W.; Sun, Z.; Liao, Y.; Liu, J.; Chen, P. Time-Varying Equivalent Power Source Modeling for High Penetration Renewable-Rich Grids. *Energies* **2026**, *19*, 3125. [CrossRef]
2. de Castro, L.C.F.; da Silva, E.C.M.; Alves, V.E.; Gonçalves, M.C.; Cantuario, J.N. From Curtailment to Energy Security: A Systematic Review of Optimization and Flexibility Strategies in High-Renewable Power Systems. *Energies* **2026**, *19*, 2981. [CrossRef]

3. Baeckeland, N.; Chatterjee, D.; Lu, M.; Johnson, B.; Seo, G.-S. Overcurrent Limiting in Grid-Forming Inverters: A Comprehensive Review and Discussion. *IEEE Trans. Power Electron.* **2024**, *39*, 14493–14517. [CrossRef]
4. Devassy, S.; Singh, B. Performance Analysis of Solar PV Array and Battery Integrated Unified Power Quality Conditioner for Microgrid Systems. *IEEE Trans. Ind. Electron.* **2021**, *68*, 4027–4035. [CrossRef]
5. Arani, Z.D.; Taher, S.A.; Guerrero, J.M. Low-voltage ride-through capability improvement in autonomous AC microgrids: A review of existing control approaches. *Renew. Sustain. Energy Rev.* **2025**, *217*, 115748. [CrossRef]
6. Rahman, K.; Hashimoto, J.; Orihara, D.; Ustun, T.S.; Otani, K.; Kikusato, H.; Kodama, Y. Reviewing Control Paradigms and Emerging Trends of Grid-Forming Inverters—A Comparative Study. *Energies* **2024**, *17*, 2400. [CrossRef]
7. Mirmohammad, M.; Azad, S.P. Control and Stability of Grid-Forming Inverters: A Comprehensive Review. *Energies* **2024**, *17*, 3186. [CrossRef]
8. He, X.; Huang, L.; Subotić, I.; Häberle, V.; Dörfler, F. Quantitative Stability Conditions for Grid-Forming Converters With Complex Droop Control. *IEEE Trans. Power Electron.* **2023**, *39*, 10834–10852.
9. Tozak, M.; Taskin, S.; Sengor, I.; Hayes, B.P. Modeling and Control of Grid Forming Converters: A Systematic Review. *IEEE Access* **2024**, *12*, 107818–107843. [CrossRef]
10. Quedan, A.; Wang, W.; Ramasubramanian, D.; Farantatos, E.; Asgarpoor, S. An Adaptive Virtual Oscillator Control Structure for Grid-Forming Inverters. *IEEE Syst. J.* **2023**, *17*, 3447–3455. [CrossRef]
11. Ghosh, R.; Tummuru, N.R.; Rajpurohit, B.S. Modified VOC Using Three Symmetrical Components for Grid-Supporting Operation During Unbalanced Grid Voltages and Grid-Forming Operation in Hybrid Single-Phase/Three-Phase Microgrid. *IEEE Trans. Ind. Electron.* **2023**, *70*, 11276–11286. [CrossRef]
12. Qiu, R.; Liu, C. Adaptive Dynamic Voltage Support Scheme for Multiple Grid-Forming Converters in Distributed Networks. *IEEE Trans. Energy Convers.* **2025**, *40*, 2624–2641. [CrossRef]
13. Tarraso, A.; Candela, J.I.; Rocabert, J.; Rodríguez, P. Selective Harmonic Compensation in SPC Grid-Forming Converters for Improving Power Quality in Weak Grid. *IEEE Trans. Power Deliv.* **2024**, *39*, 3223–3232. [CrossRef]
14. Kim, H.J.; Kim, M.S.; Lee, H.J.; Lee, E.S. Feedforward Droop Control for Reactive Power Balancing in Grid-Forming Inverters With Line Impedance Compensation. *IEEE Trans. Ind. Electron.* **2026**, *73*, 3966–3978. [CrossRef]
15. Pant, P.; Terzija, V.; Hamacher, T.; Perić, V.S. Grid Agnostic Droop Control Strategy for Damping Restoration and Optimal Reactive Power-Sharing. *IEEE Open J. Power Electron.* **2025**, *6*, 613–629. [CrossRef]
16. Kumar, B.V.; Farhan, M.A.A. Multi-objective optimization framework for strategic placement of electric vehicle charging stations and shunt capacitors in a distribution network considering traffic flow. *Appl. Energy* **2025**, *397*, 126284. [CrossRef]
17. Nazih, A.; El-Ela, A.A.A.; Ali, E.S. Maximizing hosting capacity of renewable energy sources in unbalanced distribution networks using multi-objective optimization approach. *Electr. Power Syst. Res.* **2025**, *241*, 111342. [CrossRef]
18. Cortés-Caicedo, B.; Grisales-Noreña, L.F.; Montoya, O.D.; Bolaños, R.I.; Muñoz, J. A multi-objective optimization approach based on the Non-Dominated Sorting Genetic Algorithm II for power coordination in battery energy storage systems for DC distribution network applications. *J. Energy Storage* **2025**, *113*, 115430. [CrossRef]
19. Shaheen, M.A.M.; Hasanien, H.M.; Alsaleh, I.; Alassaf, A.; Zhang, M.; Alateeq, A. Optimal Power Flow in Power Systems with Renewable Energy Resources Uncertainty Including Geothermal Power Plants. *Ain Shams Eng. J.* **2025**, *16*, 103784. [CrossRef]
20. Shaheen, M.A.M.; Ullah, Z.; Qais, M.H.; Hasanien, H.M.; Chua, K.J.; Tostado-Véliz, M.; Turky, R.A.; Jurado, F.; Elkadeem, M.R. Solution of Probabilistic Optimal Power Flow Incorporating Renewable Energy Uncertainty Using a Novel Circle Search Algorithm. *Energies* **2022**, *15*, 8303. [CrossRef]
21. Dimara, A.; Papaioannou, A.; Grigoropoulos, K.; Triantafyllidis, D.; Tzitzios, I.; Anagnostopoulos, C.-N.; Krinidis, S.; Ioannidis, D.; Tzovaras, D. A Novel Real-Time PV Error Handling Exploiting Evolutionary-Based Optimization. *Appl. Sci.* **2023**, *13*, 12682. [CrossRef]
22. Feng, W.; Zhang, W.; Huang, S. A Novel Parameter Estimation Method for PMSM by Using Chaotic Particle Swarm Optimization With Dynamic Self-Optimization. *IEEE Trans. Veh. Technol.* **2023**, *72*, 8424–8432. [CrossRef]

Disclaimer/Publisher's Note: The statements, opinions and data contained in all publications are solely those of the individual author(s) and contributor(s) and not of MDPI and/or the editor(s). MDPI and/or the editor(s) disclaim responsibility for any injury to people or property resulting from any ideas, methods, instructions or products referred to in the content.